CEAS Space J (2015) 7:347–358
DOI 10.1007/s12567-015-0083-3

ORIGINAL PAPER

ARCADE-R2 experiment on board BEXUS 17 stratospheric balloon

Marco Barbetta[1] · Alessandro Boesso[2] · Francesco Branz[3] · Andrea Carron[1] · Lorenzo Olivieri[3] · Jacopo Prendin[4] · Gabriele Rodeghiero[5] · Francesco Sansone[3] · Livia Savioli[3] · Fabio Spinello[1] · Alessandro Francesconi[6]

Received: 6 November 2014 / Revised: 6 March 2015 / Accepted: 6 March 2015 / Published online: 31 March 2015

Abstract This paper provides an overview of the ARCADE-R2 experiment, a technology demonstrator that aimed to prove the feasibility of small-scale satellite and/or aircraft systems with automatic (a) attitude determination, (b) control and (c) docking capabilities. The experiment embodies a simplified scenario in which an unmanned vehicle mock-up performs rendezvous and docking operations with a fixed complementary unit. The experiment is composed by a supporting structure, which holds a small vehicle with one translational and one rotational degree of freedom, and its fixed target. The dual system features three main custom subsystems: a relative infrared navigation sensor, an attitude control system based on a reaction wheel and a small-scale docking mechanism. The experiment bus is equipped with pressure and temperature sensors, and wind probes to monitor the external environmental conditions. The experiment flew on board the BEXUS 17 stratospheric balloon on October 10, 2013, where several navigation-control-docking sequences were executed and data on the external pressure, temperature, wind speed and direction were collected, characterizing the atmospheric loads applied to the vehicle. This paper describes the critical components of ARCADE-R2 as well as the main results obtained from the balloon flight.

Keywords Docking mechanism · IR navigation · Autonomous miniature vehicles · Stratospheric balloon experiment

✉ Marco Barbetta
barbettamarco@gmail.com

✉ Lorenzo Olivieri
olivieri.lrnz@gmail.com

[1] Department of Information Engineering, University of Padova, Padova, Italy

[2] Vitrociset Belgium SPRL, Transinne, Belgium

[3] Centre of Studies and Activities for Space "G. Colombo", University of Padova, Padova, Italy

[4] Department of Computer Science, University of Venice, Venice, Italy

[5] Department of Physics and Astronomy, University of Padova, Padova, Italy

[6] Department of Industrial Engineering, University of Padova, Padova, Italy

1 Introduction

In the last decade, there has been a considerable interest in the development of highly capable, autonomous small-scale vehicles for both space and aeronautic applications.

On one hand, as regards the space field, the employment of miniature spacecraft with advanced capabilities could improve the execution of several new missions, including: (a) on-orbit automated inspection and servicing of larger satellites, in order to extend their operational lifetime, replace their payloads or perform orbital manoeuvres [1, 2]; (b) on-orbit assembly of low-cost large modular spacecraft that would significantly benefit from standardization and miniaturization of the used modules, as well as from the possibility of launching them as piggybacks [3, 4]; (c) debris capture and active removal [5, 6].

On the other hand, advanced cooperative micro aerial vehicles (MAVs) could be employed in several atmospheric applications, e.g. (a) remote observation of hazardous or otherwise unreachable areas, i.e. toxic regions, urban canyons or interior of buildings, (b) evaluation, rescue and surveillance operations.

In most of the current demonstrative applications, regarding both space and aerial fields, small spacecraft or vehicles are usually supported by a larger parent, which is dedicated to communication management, coordination and refuelling and/or refurbishment operations. In this scenario, proximity autonomous navigation and attitude control subsystems, together with docking devices, represent the main qualifying technologies but, while they have already been developed for large space or air vehicles, there is still a lack of applicable solutions for miniaturized automatic systems [7–10].

This paper presents the evolved version of the experiment ARCADE [11], named ARCADE-R2, which was developed at the Centre of Studies and Activities for Space "CISAS G. Colombo"—University of Padova. ARCADE-R2 aimed to test autonomous navigation, attitude control and docking technologies in an extreme environment on-board a stratospheric balloon in the REXUS/BEXUS Program, in the wider framework of CISAS researches on automatic docking technologies [12, 13]. The experiment is developed with the following objectives: (a) test the custom-designed subsystems required to perform relative proximity navigation, relative attitude control and docking between a small aerial vehicle and its parent counterpart mounted on the BEXUS gondola; (b) evaluate the disturbances that affect control and docking operations at different altitudes during the ascent phase of the BEXUS balloon; (c) relate the navigation, control and docking systems performances to the experienced disturbances; (d) repeat several navigation-control-docking sequences in the low-disturbances environment expected in the float phase.

This paper is organized as follows: first, the experiment layout is presented in Sect. 2, while the main subsystems—docking mechanism, control system and relative navigation sensor—are described in details in Sects. 3, 4 and 5, respectively; some brief information on the support hardware of the experiment can be found in Sect. 6.

2 Experiment layout

During BEXUS-17 mission, autonomous docking sequences were attempted in extreme environment conditions between a small external vehicle, called SMAV (SMAll Vehicle), and its parent unit, named PROXBOX (PROXimity BOX). The PROXBOX is designed to be mounted on the balloon gondola, which is the main structure lifted by the BEXUS balloon and where the scientific experiments are placed. The SMAV, on the other hand, is supported by an external rigid structure, called STRUT (STRUcTure), which connects the small vehicle to the gondola (Fig. 1). The SMAV represents the chaser vehicle in the simulated docking scenario. It hosted dedicated

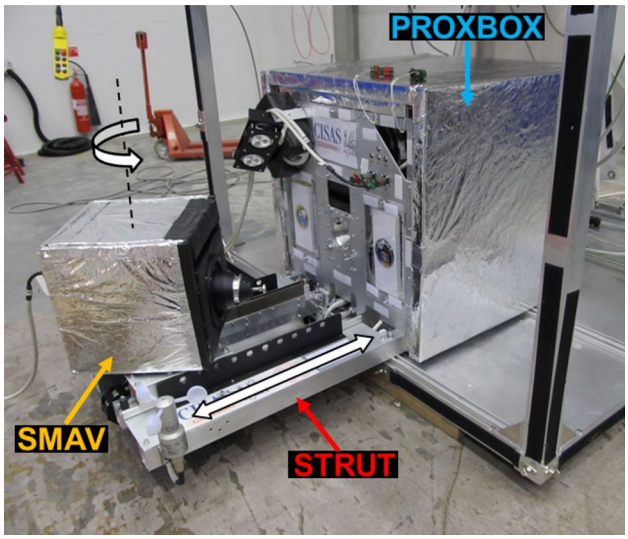

Fig. 1 ARCADE Experiment main elements and degrees of freedom

navigation, control and docking devices as well as an eight-cell battery that makes it a power independent vehicle. It relies, however, on the PROXBOX flight computer for data processing. The SMAV has two controlled degrees of freedom (DoF): a rotational DoF around the vertical yaw axis, and a translational DoF towards the gondola. All the remaining DoFs are fixed.

The STRUT houses the devices needed to translate the SMAV and safely connects the external vehicle to the gondola. In particular, the small vehicle is mounted on a mobile supporting interface (SMAV-STRUT interface) that allows rotating and translating the SMAV while ensuring mechanical connection. The STRUT also holds a set of sensors to sound the external environment.

The PROXBOX represented the target in the reproduced docking scenario, and it was mounted on the gondola with a wall facing outwards. It contains the parent-vehicle docking interface and navigation transmitters, a dedicated battery pack, most of the experiment electronics and the main processing unit. It handles the data sampling, receives commands, sends telemetry/data to the ground station, provides data storage and manages all the experiment devices and sensors.

3 Docking mechanism

The ARCADE-R2 probe-drogue docking subsystem (Fig. 2) can be classified as small-scale, central and gender-mating. It is based on the concept of the Soyuz and ATV docking systems, and it is realized through the employment of commercial components, making it low-cost and simple to be manufactured.

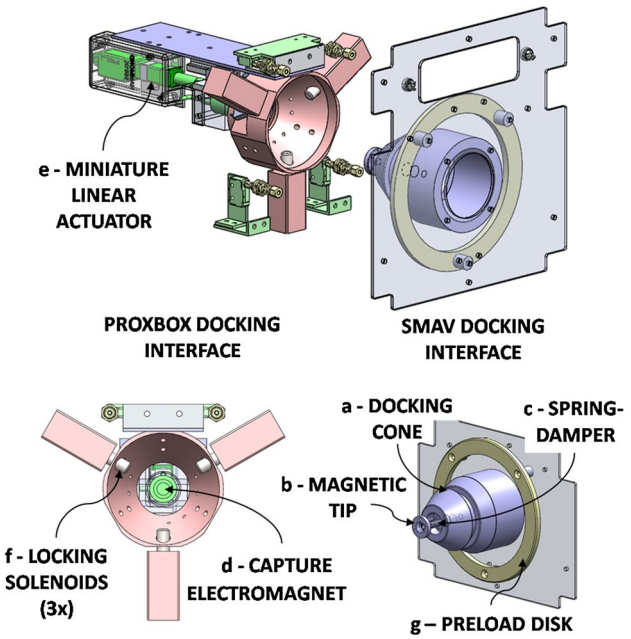

Fig. 2 ARCADE docking system: the gender-mate mechanism is composed by two interfaces (the drogue on the PROXBOX, actuated by a miniature linear actuator, the probe on the SMAV); three solenoids create the solid joint in hard docking configuration

The first interface (probe) is mounted in front of the SMAV and is totally passive. It presents a conical shape (a) with a magnetic tip (b) mounted on a spring-damper (c) to absorb contact forces during docking procedures. The drogue is attached on the external wall of the PROXBOX, and it presents a conical shape to match that of the probe. The docking sequence is initiated by a "soft docking", in which the probe is captured by a small electromagnet installed at the end of the drogue (d). Then, thanks to a miniature linear actuator (e), the SMAV is pulled towards the PROXBOX until the two interfaces are mated. The procedure is completed by a "hard docking", in which structural connection is achieved by means of three peripheral solenoids (f). In addition, a spring-mounted disc, installed on the SMAV side, is loaded during the mating of the two interfaces (g). It allows to both create a compressive force that further secures the joint in the "hard docking" configuration and to push away the SMAV during the release phase.

3.1 Numerical simulations

The ARCADE docking mechanism is extensively verified through numerical simulations to define the dynamical behaviour of the interfaces in both nominal and off-nominal condition and to investigate the maximal allowable misalignment to successfully perform the joining operation [11]. Simulations are performed with the multi-body dynamics analysis software MD ADAMS 2010, collecting enough data to validate and accept the design process before the launch campaign. Results indicate that both capture and structural connection correctly take place at a velocity of 50 mm/s, even with a yaw misalignment of 5° and with a residual rotation rate of 0.5° s^{-1}. In this case, however, the SMAV showed an oscillating behaviour prior to the structural locking, suggesting that these values, located at the boundary of the desired docking envelope, truly represent its limits. It is also verified that docking sequences featuring a higher approach velocity, 100 mm/s, or a greater misalignment, 10°, do not succeed.

Dynamical simulations are validated by laboratory tests, demonstrating that the system features a good tolerance to misalignments from nominal docking conditions, in which the main axis of the two interfaces is aligned. Numerical results and laboratory data are used to set the experimental limits for the stratospheric flight tests.

3.2 Pre-flight and flight data

During the integration on the BEXUS gondola, ARCADE-R2 was continuously subjected to test. Data collected during such trials confirmed functionality of all the docking actuators and sensors prior to flight and permitted to check the nominal alignment between the docking interfaces. In this phase, the automatic docking procedure was calibrated, measuring for each motor the required actuation to perform their tasks, and comparing them with laboratory data, in order to check whether the experiment was revealing any residual deformation after the transportation to Esrange Space Center. The subsystem was declared ready to flight and was launched in the mated configuration, in order to reduce the transient loads that could affect the motors, and was released at 18:20 (local time) to perform its programmed procedures.

During the flight, ARCADE-R2 successfully performed three release operations and two docking procedures (Fig. 3). In the first flight test, it was observed that the drogue actuator was not able to capture the probe, probably because of minimal thermal deformations in ARCADE-R2 (the temperature dropped of about 1.55 °C every minute for the first 30 min). Furthermore, this failure was not correlated to wind disturbances, since such torques were almost constant during all the three docking tests (see Fig. 15). In fact, the linear actuator behaviour at low temperature slightly differed with respect to the behaviour at room temperature because of variation of its internal viscous friction; for this reason, the miniature linear actuator was not able to reach the desired position and the contact between drogue and probe was not optimal. Anyway, it was sufficient to increase the linear actuator set point by 1 mm to allow a

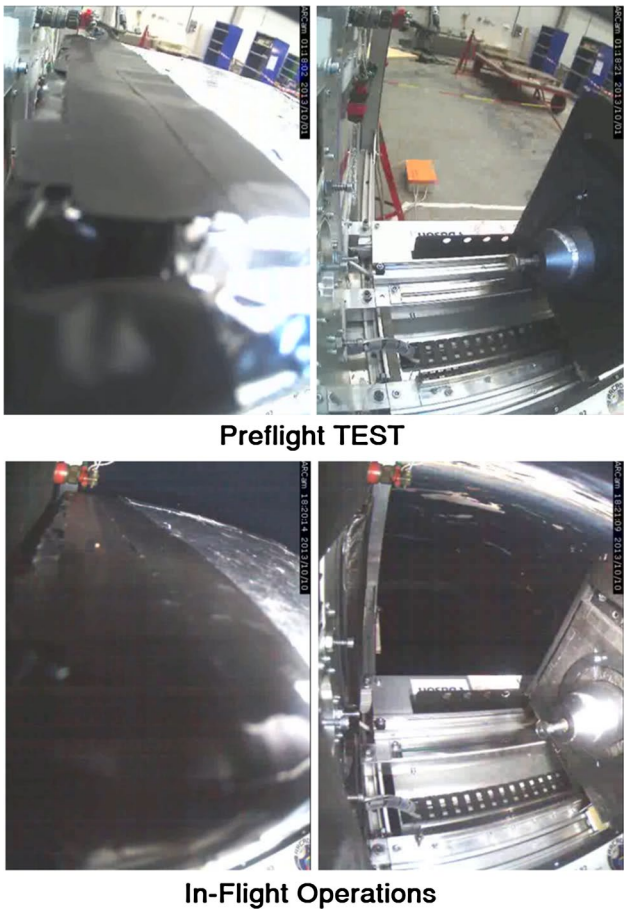

Fig. 3 ARCADE-R2 docking procedures during pre-launch test (*top*) and flight (*bottom*); ARCADE successfully performed three releases and two docking procedures during the flight

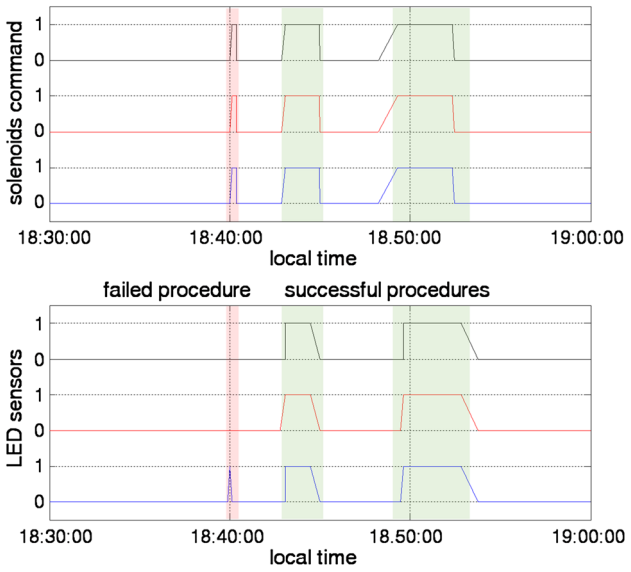

Fig. 4 During the first docking procedure, on-board sensors showed that two of the electromagnetic latches (command signal, *up*), although commanded, did not lock the mechanism (sensors signal, *down*); increasing the miniature linear actuator set point allowed solving this issue and perform two docking manoeuvres

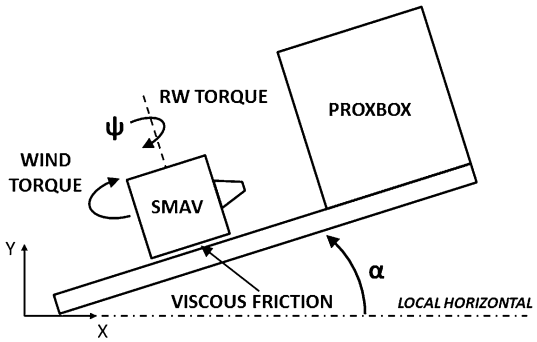

Fig. 5 Illustration of the forces and the torques involved in the ARCADE dynamic model

better contact between the probe and the drogue and realize two complete docking sequences (Fig. 4).

Collected data, however, demonstrate the mechanism intrinsic robustness and confirm the design process; future works may improve the docking interfaces to reduce the mass utilization and the power budget, possibly introducing passive hard docking latches. Last, the whole design process and the data collected during the flight give important suggestions for similar docking systems developed at CISAS in the framework of small satellites docking system development [12–14].

4 Motion control system

The main task of the ARCADE-R2 Control Subsystem is to actively control the yaw movements of the SMAV, thus permitting the SMAV-PROXBOX alignment. A correct attitude is required while approaching the PROXBOX in order to successfully complete the docking manoeuvres, although the docking mechanism was designed to tolerate a maximum misalignment of ±5°. For this purpose, two alternative electric actuators are employed: (a) a custom reaction wheel (RW) on board the SMAV and (b) a brushless DC motor directly connecting the SMAV to the support plate. The first is the nominal actuator for realistic operations, while the second is a backup solution.

Two alternative solutions are implemented also for the experiment motion control software: (a) a state-space control and (b) a simple PID control law. The control algorithms are designed considering the SMAV angular position/velocity and the reaction wheel speed. Gravitational torques due to the gondola roll and pitch oscillations can be predicted and are rejected in feedforward (see Sect. 4.1).

On the attitude determination side, two options are also implemented in the experiment: (a) the custom IR navigation sensor (see Sect. 5) and (b) an optical encoder coupled with the backup motor.

Figure 5 illustrates the forces and torques considered in the model. The linear motion of the SMAV is driven at a constant speed, which is reached through a smooth acceleration; consequently, the SMAV linear acceleration is limited and the inertial torque disturbance on the SMAV is neglected. The differential equation that governs the SMAV angular acceleration is reported in Eq. 1.

$$I\ddot{\theta} = mge[\sin\alpha \sin(\psi - \psi_0 - \pi) + \sin\beta \times \sin\left(\psi + \psi_0 - \frac{\pi}{2}\right)] + \tau_w - \mu_f\dot{\theta} + \tau_m \tag{1}$$

where I is the moment of inertia of the SMAV, m is the mass of the SMAV, g is the gravity acceleration, α is the gondola pitch misalignment, β is the gondola roll misalignment, ψ is the SMAV yaw rotation, ψ_0 is the centre of mass angular position of the SMAV, e is the centre of mass eccentricity, τ_w is the wind disturbance torque, μ_f is the viscous friction coefficient, τ_m is the input torque provided by the reaction wheel.

4.1 State-space controller

The SMAV dynamic system, Σ_c, written in continuous state-space form is presented in Eq. 2, neglecting the disturbances.

$$\begin{cases} \dot{x}(t) = Ax(t) + Bu(t) \\ y(t) = Cx(t) + Du(t) \end{cases}$$
$$A = \begin{bmatrix} 0 & 1 \\ 0 & -\frac{\mu_f}{I} \end{bmatrix} \quad B = \begin{bmatrix} 0 \\ \frac{1}{I} \end{bmatrix} \quad C = \begin{bmatrix} 1 & 0 \end{bmatrix} \quad D = 0 \tag{2}$$

where A, B, C and D are matrices of suitable dimensions, μ_f is the viscous friction coefficient, I is the SMAV inertia, $x = \begin{bmatrix} \psi & \dot{\psi} \end{bmatrix}^T \in \mathbb{R}^2$ is the state vector while u and y are the system input (i.e. reaction wheel torque) and output (i.e. yaw angle), respectively.

The design steps to obtain a discrete state-space controller using the output feedback are: (a) conversion of the continuous time system to discrete time, (b) design of the state feedback controller, (c) design of the state observer and (d) implementation of an integral controller and a feedforward controller.

4.1.1 Discrete time conversion

It is necessary to convert the continuous time system, Σ_c, to a discrete one, Σ_d, which is capable to predict the output of the original system at each sample instant. Calling T the sample time, the update law is given by

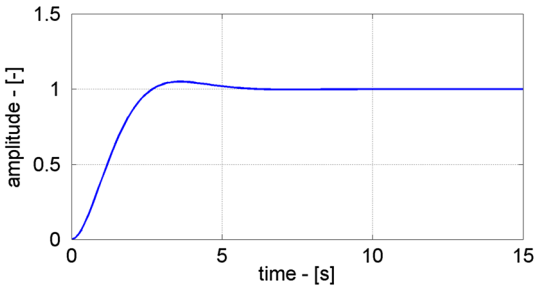

Fig. 6 Target step response of the controlled system (*closed loop*)

$$x(k+1) = Fx(k) + Gu(k)$$
$$y(k) = Cx(k) + Du(k) \tag{3}$$

where

$$F = e^{AT}$$
$$G = \int_0^T e^{At}Bdt \tag{4}$$

4.1.2 Discrete time controller

After checking the system controllability and calculating the state feedback gain, K, the eigenvalues are placed with the following specifications:

- rise time $t_r = 3$ s
- settling time $t_s = 4$ s
- maximum overshoot $m_p = 5$ %

From these constraints, the denominator, $d(s)$, of the controlled system target transfer function is computed (see Fig. 6 for the target step response). The roots of $d(s)$ are the poles of the controlled system in continuous time form and are used to compute the discrete time system poles with the zero-pole matching technique.

4.1.3 State observer

The state is not known and might not correspond to a real quantity; therefore, a state observer is needed. Being the described model deterministic, a Luenberger observer is chosen. Its implementation is straightforward (Eq. 5).

$$\hat{x}(k+1) = A\hat{x}(k) + L\left[y(k) - C\hat{x}(k)\right] - B\hat{x}(k) \tag{5}$$

where L is chosen in order to have the eigenvalues of A-LC ten times smaller than the eigenvalues of the closed loop system. This is because the observer has to converge to its steady state value faster than the controller.

4.1.4 Integral and feedforward controller

In order to track step inputs, the internal model control technique is implemented; it consists in embedding the controller with a single integrator and a copy of the signal to track.

The design of the integral gain is made in parallel with the state feedback gain K on the augmented system (Eq. 6) obtained by adding the integrator. The additional pole is placed in one.

$$F_{\text{aug}} = \begin{bmatrix} 1 & C \\ 0 & F \end{bmatrix}$$

$$G_{\text{aug}} = \begin{bmatrix} 0 \\ G \end{bmatrix} \tag{6}$$

The pitch and roll oscillations of the gondola α and β determine gravitational torques on the SMAV due to centre of mass misalignment. These disturbances are rejected outside the feedback loop thanks to the measurements provided by an inclinometer located inside the PROXBOX and by a linear encoder. The angle measurements allow predicting the disturbance torque and actuating the RW before the external torques affect the SMAV attitude. A feedforward compensation is designed to perform such rejection. The complete control system scheme is shown in Fig. 7.

4.2 PID controller

The second solution for the SMAV motion control is a simple discrete PID. The parallel structure is chosen for its simplicity. The update law is the following:

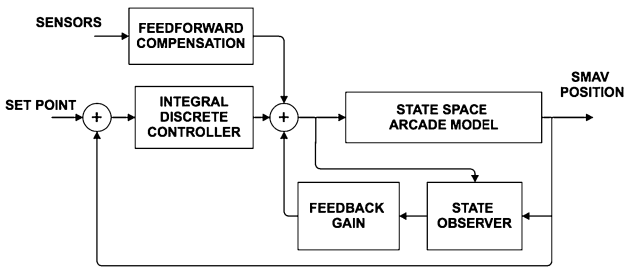

Fig. 7 Logic scheme of the state-space controller

$$u(k) = K_{\text{p}} e(k) + \frac{K_i}{T} \sum_{i=0}^{k} e(i) + \frac{K_{\text{d}}}{T} [e(k) - e(k-1)] \tag{7}$$

where $e(k)$ is the difference between the set point and the output $y(k)$, K_{p}, K_i and K_{d} are the proportional, integral and derivative gains, respectively. The three gains are computed through analytical computations and then tuned manually.

4.3 Experimental results

As already mentioned, different options are available on ARCADE-R2 regarding the SMAV yaw actuation, the feedback sensors and the control algorithm. Table 1 lists in horizontal lines the four tested combinations of these options during BEXUS-17 flight (#1 to #4).

The feedback loop on the backup motor is a PID position loop internal to the motor driver; it is not possible to control it with the custom controllers developed for ARCADE-R2.

Unfortunately, the SS feedback loop combined with the IR sensor feedback showed to be unreliable during preflight tests and, consequently, was not included within the flight operations.

During the mission, the backup motor positioning always worked properly. Several homing and pointing manoeuvres were executed during the flight (test #1, see Table 1), and the accuracy was always within the target performances. Figure 8 shows the results of an example manoeuvre.

The reaction wheel control with the encoder feedback worked properly during the two tested manoeuvres, one with PID controller (test #2) and one with SS controller (test #3). A $\pm 4°$ dead band is implemented in order to avoid the saturation of the RW. Figure 9 shows the pointing angle with RW actuation, encoder feedback and PID controller, while Fig. 10 shows the pointing with SS controller. Some manoeuvres were tried on the IR sensor feedback, but the results were not satisfactory (test #4). This was due to a non-optimal calibration of the IR sensor estimation algorithm before launch (more in Sect. 5.3). Figure 11 shows the yaw angle vs. time for one of these manoeuvres.

Table 1 Matrix of motion tests executed during BEXUS-17 flight

	Actuation		Sensors		Algorithm	
	RW	BM	IR	E	SS	PID
#1		X		X	–	–
#2	X			X		X
#3	X			X	X	
#4	X		X			X

RW reaction wheel, *BM* backup motor, *IR* infrared sensor, *E* optical encoder, *SS* state-space controller, *PID* PID controller

5 Navigation system

The experiment is provided with a custom relative navigation sensor for the determination of the SMAV linear position and yaw rotation, with respect to the PROXBOX docking interface.

5.1 Sensor layout

The sensor design aims at compactness and simplicity, both in terms of hardware components and software computational burden. In particular, the sensor is conceived as an alternative to systems based on image processing or LIDARs [15–18].

As a result, the sensor is composed by a beacon infrared LED on-board the PROXBOX and two infrared photodiode receivers mounted on the face of the SMAV containing the docking mechanism (see Fig. 12). The working principle is very simple: the photodiodes output voltages generated by the LED beacon are modulated by the SMAV—PROXBOX relative position and attitude and are measured with high accuracy; then, a dedicated algorithm based on the LED emission model and the experiment geometry determines the SMAV position and attitude relative to the PROXBOX from the measured signals. The distance between the two infrared receivers was set in order to generate a significant difference in the photodiode voltages due to rotation, while keeping them within the emission lobe of the beacon.

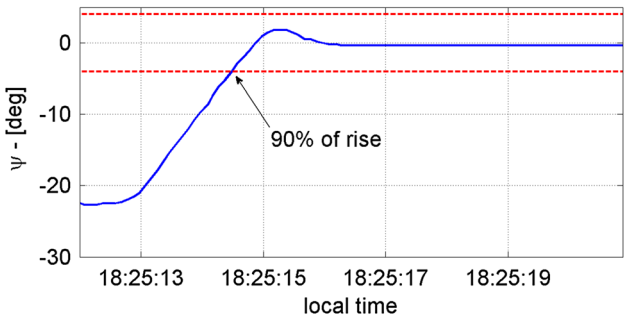

Fig. 8 SMAV pointing manoeuvre: backup motor on encoder feedback (test #1)

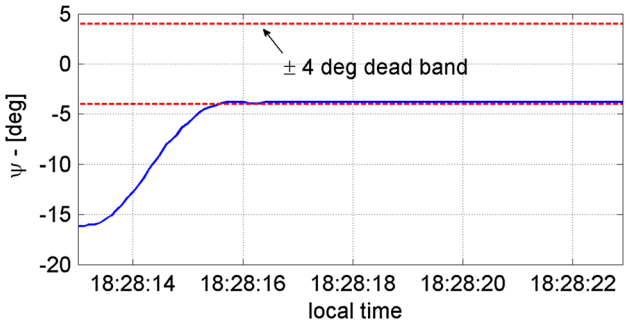

Fig. 9 SMAV pointing manoeuvre reaction wheel on encoder feedback, PID controller (test #2)

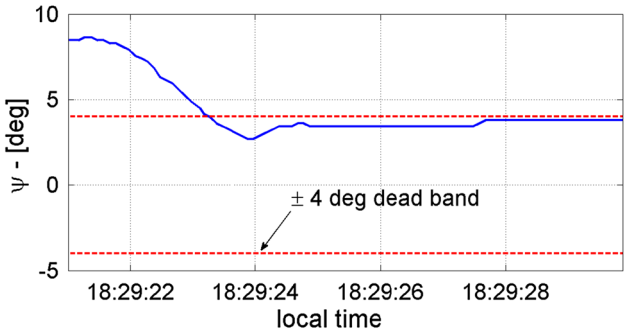

Fig. 10 SMAV pointing manoeuvre: reaction wheel on encoder feedback, SS controller (test #3)

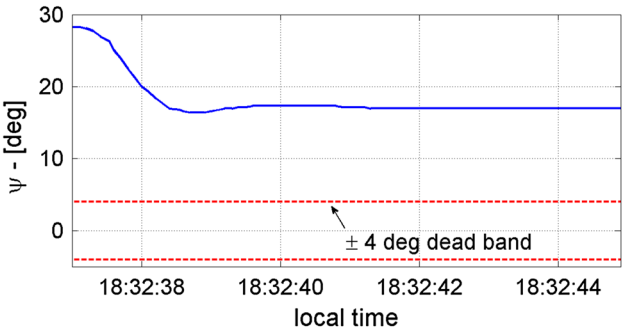

Fig. 11 SMAV pointing manoeuvre: reaction wheel on IR sensor feedback, PID controller (test #4)

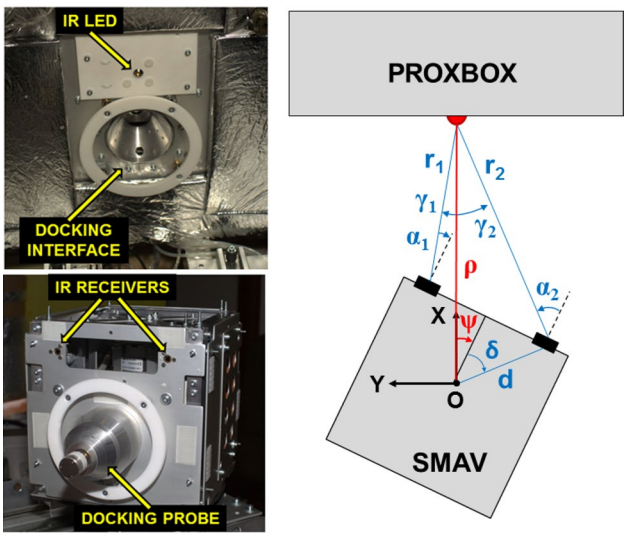

Fig. 12 Elements of the IR sensor on the PROXBOX (*top left*) and on the SMAV (*bottom left*) and geometrical parameters of the sensor model (*right*)

From the hardware point of view, particular attention was paid to the rejection of ambient light that could affect the sensor measurements. For this reason, photodiodes with daylight filter are exploited and the beacon emission is distinguished from direct sunlight by modulating the LED drive current with a 10-kHz sinusoid. The receiver conditioning boards use amplifiers with a narrow band-pass filter centred at 10 kHz followed by precision envelope detector.

Temperature issues affecting gain stability are taken into account in both transmitter and receiver electronics design. The LED emission level is kept constant thanks to a precision sinusoidal current source featuring a power op-amp with current shunt feedback as output stage; the shunt is characterized by high temperature stability. The gain of the receiver section can be adjusted in order to match the signal dynamics due to distance and yaw angle ranges. In order to assure high receiver gain stability, the photodiode conditioning boards employ high-stability op-amp integrated circuits, precision feedback resistors and high op-amp feedback.

5.2 Sensor model

The photodiode output voltages V_i ($i = 1, 2$) are described in Eqs. 17 and 18; they depend on the power emitted by the LED P_{LED}, the LED-photodiode distance r_i, the photodiode sensitive area A_i, the photodiode photosensitivity k_i, the angle of incidence α_i, the angle γ_i between the LED optical axis and the line joining the LED to the i-th photodiode, and the amplification gain of the receivers conditioning electronics e_i. The term $f(\gamma)$ represents the ratio between the LED radiant intensity (Wsr^{-1}) at a given γ and the radiant intensity at $\gamma = 0$. Both $f(\gamma)$ and $g(r)$ were determined experimentally by fitting the photodiode outputs that were measured during laboratory tests prior the launch campaign. Moreover, the amplification contribution of the acquisition channel of each infrared receiver can be defined as $C_i = P_{\mathrm{LED}} A_i k_i e_i$. Such terms are independent from the SMAV position and attitude; however, they are modified by the environment temperature variation, as the latter affects the photodiode sensitivity k and the forward voltage of the LED. For this reason, the C_i parameters are periodically calibrated.

The system is mathematically described by Eqs. 8–14. As the translational motion of the SMAV can occur only along the LED central axis direction, the parameters r_i, α_i and γ_i result from simple geometrical relations involving the SMAV distance ρ and yaw rotation ψ relative to the PROXBOX. The values of d and δ are known from the geometry of the SMAV. By combining Eqs. 8–14, the analytical expressions $V_1(\rho, \psi)$ and $V_2(\rho, \psi)$ can be obtained, which describe the receivers outputs as function of solely the SMAV distance ρ and yaw rotation ψ.

$$V_1 = P_{\mathrm{LED}} A_1 k_1 e_1 f(\gamma_1) g(r_1) \cos\alpha_1 = C_1 f(\gamma_1) g(r_1) \cos\alpha_1 \tag{8}$$

$$V_2 = P_{\mathrm{LED}} A_2 k_2 e_2 f(\gamma_2) g(r_2) \cos\alpha_2 = C_2 f(\gamma_2) g(r_2) \cos\alpha_2 \tag{9}$$

$$r_{1,2} = \sqrt{\rho^2 + d^2 - 2\rho d \cos(\psi \mp \delta)} \tag{10}$$

$$\gamma_{1,2} = \tan^{-1}\left[\frac{d \sin(\psi \mp \delta)}{\rho - d\cos(\psi \mp \delta)}\right] \tag{11}$$

$$\alpha_{1,2} = \gamma_1 \mp \psi \tag{12}$$

$$f(\gamma) = 1 - k_1\gamma^2 - k_2\gamma^{10} \tag{13}$$

$$g(r) = a_1 \sin(b_1 r + c_1) + a_2 \sin(b_2 r + c_2) \tag{14}$$

The flight software of the experiment exploits an inversion iterative algorithm based on the Gauss–Newton method in order to determine ρ and ψ from the measured photodiode voltages. The algorithm is described in Eqs. 15–18. The 2D nonlinear problem is formulated as follows, considering the sensor model:

$$\bar{y} = \begin{bmatrix} V_1(\bar{x}) \\ V_2(\bar{x}) \end{bmatrix} = G(\bar{x}), \quad (\bar{x}) = (\rho, \psi) \tag{15}$$

The iterative process updates an initial guess for (ρ, ψ) according to Eqs. 16–17, until the difference between the measured voltages y_{measured} and $y(\bar{x}_k)$ is lower than a preset threshold. The solution found is then fed to the algorithm as initial guess for the subsequent estimation process. The parameter J_k (Eq. 18) is the Jacobian matrix of the nonlinear system, whose analytical expression was calculated using a commercial software for symbolic computation.

$$\Delta\bar{x}_k = \left(J_k^T J_k\right)^{-1} J_k^T \left[y_{\mathrm{measured}} - y(\bar{x}_k)\right] \tag{16}$$

$$\bar{x}_{k+1} = \bar{x}_k + \Delta\bar{x}_k \tag{17}$$

$$J(\bar{x}) = \frac{\partial G_i}{\partial X_j} = \begin{bmatrix} \frac{\partial V_1(\rho,\psi)}{\partial \rho} & \frac{\partial V_1(\rho,\psi)}{\partial \psi} \\ \frac{\partial V_2(\rho,\psi)}{\partial \rho} & \frac{\partial V_2(\rho,\psi)}{\partial \psi} \end{bmatrix} \tag{18}$$

The Gauss–Newton method was selected for its simplicity and fast convergence. The solution is always found in less than 10 steps.

More details and the description of an alternative algorithm based on look-up tables can be found in [19].

5.3 Experimental results

The infrared navigation sensor was tested during various automatic procedures that were executed by the experiment

during the flight. At the beginning of each of them, the calibration constants of the photodiode receiver acquisition channels, C_1 and C_2, were determined automatically. This solution was adopted as both the LED emitter and the photodiode receivers are sensitive to temperature variations, requiring a periodic calibration during the whole flight. Then, the reconstruction algorithm was applied to the measured photodiode voltages, providing a real-time estimation of the SMAV distance ρ and yaw rotation ψ relative to the PROXBOX. The relative navigation sensor performance is expressed in terms of standard deviation σ_ρ, σ_ψ of the estimates of ρ and ψ with respect to reference values given by the linear and rotary encoders mounted on the experiment. The estimates of ρ and ψ determined during the flight are characterized by uncertainties σ_ρ and σ_ψ of 17 mm and 2.7°, respectively. It is important to notice that these are average values, and the actual uncertainty can be better or worse depending on the actual values of ρ and ψ.

Data collected during the flight were also analysed in post-processing. A refined model of the LED emission was obtained, providing a better fitting of the infrared photodiode receivers output. Moreover, an improved version of the estimation algorithm was implemented, based on the Levenberg–Marquardt method [20, 21].

Then, the inversion algorithm was applied again to the receivers signals measured and recorded during the flight.

The sensor performance assessment in post-processing gave better results, compared to the flight data. In fact, the uncertainty of the estimates of ρ and ψ is improved to 5 mm and 1.5°, respectively. As stated above, these are average values of σ_ρ and σ_ψ. In particular, a worsening of sensor performance of ~50 % is noticed for ψ approaching its range limits (±40°) and for low values of ρ (0.23 m), which means the SMAV tip is being captured by the drogue. In both cases, the photodiode receivers are close to the lateral limits of the LED lobe, which causes signal attenuation. For low values of ψ and higher values of ρ, the uncertainty is better than the average values (~50 %).

Figure 13 shows the results of the estimation process compared to the values of SMAV position and attitude provided by the encoders, and indicates the instants when the calibration constants were determined.

The sensor performance assessment in post-processing gave better results, compared to the flight data. In fact, the uncertainty of the estimates of ρ and ψ is improved to 5 mm and 1.5°, respectively. As stated above, these are average values of σ_ρ and σ_ψ. In particular, a worsening of sensor performance of ~50 % is noticed for ψ approaching its range limits (±40°) and for low values of ρ (0.23 m), which means the SMAV tip is being captured by the drogue. In both cases, the photodiode receivers are close to the lateral limits of the LED lobe, which causes signal attenuation. For low values of ψ and higher values of ρ, the uncertainty is better than the average values (~50 %).

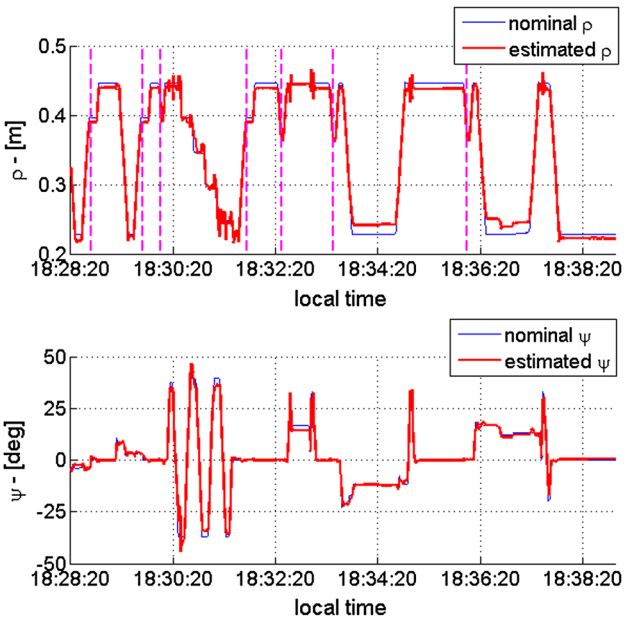

Fig. 13 Estimates of the SMAV-PROXBOX relative distance ρ (*top*) and SMAV yaw rotation ψ (*bottom*) compared to the reference values given by the linear and rotary encoders. The *dotted vertical lines* indicate when the calibration constants were determined

6 Support bus

The scientific payload is supported by the experiment bus in order to survive, operate, communicate and monitor the operative conditions. The support bus is composed by the electronic, power, software, thermal control and environmental sensors subsystems.

6.1 Electronic subsystem

The electronic system is conceived keeping in mind the need to control many types of actuators and to acquire different types of physical measurements. Therefore, an industrial CANopen bus solution is adopted. Most of the selected devices are CANopen compatible and are queried by the main intelligence of the system, an x86-based PC104 single-board computer (SBC).

The SBC board contained a real-time QNX OS, which executed management, telecommand and telemetry tasks. All the data acquisition (sensors, diagnostic currents, voltages, switch status) and actuation (motors, transmitters and latches) is performed through industrial automation modules and motor drivers connected to the SBC through the CANopen bus.

An analog sine wave generator followed by an impressed-current driver powers the LED emitter on board of the PROXBOX. Signal from the photodiode receiver on board of the SMAV is conditioned, demodulated and acquired by CANopen compatible modules.

The electronic system experienced no failures during BEXUS-17 flight, neither on signal conditioning nor on actuator operation.

6.2 Power subsystem

Because of the mechanical structure of the experiment, the power systems of PROXBOX and SMAV are isolated and totally independent. The power source consisted of Li-$SOCl_2$ (Lithium Thionyl-Chloride) battery packs (total energy 1.3 kWh, nominal).

Both the SMAV and the PROXBOX power systems are equipped with current and voltage diagnostics in order to monitor the battery and subsystem voltages and the current consumption.

During the flight, the power system sustained the power needs of each experiment subsystem as expected, and the reserve power on the batteries kept the SBC running until recovery.

6.3 Software subsystem

The software design involves two segments: the flight segment, operating on the SBC, and the ground segment, running on GSE computers, interconnected by the E-Link (a long-range radio link provided by the balloon flight support equipment). The flight segment software is designed to autonomously perform experiment test procedures and manage data storage on a solid state memory and telemetry relay to ground segment. The ground segment allows manual telecommand of experiment operation and retrieves/displays real-time telemetry.

The software system experienced no failures or crashes, correctly delivered telemetry and granted telecommand access throughout the mission duration.

6.4 Thermal control subsystem

The thermal control subsystem is mainly passive with some heaters to keep the most critical experiment components (motor drivers, batteries, actuators, etc.) within operative temperatures. A total of 25 heaters (Conflux HF-20-1003) with 2 W of power output are mounted on the experiment. The heat flux generated by such heaters varies according to a linear function of the ambient temperature, i.e. the lower the temperature, the greater the generated heat, resulting in a self-regulating system. In addition, 8-W heaters (Conflux HF-30-1009) are used during pre-flight operations to keep the system warm on the launch pad.

Despite the extremely low external temperature during BEXUS-17 flight, the temperatures inside the experiment remained within the operative ranges for the whole mission and no controlled component showed malfunctions due to low temperature.

6.5 Environmental sensors subsystem

Operative conditions of the experiment are monitored with wind, pressure and temperature sensors.

Wind direction and intensity in the horizontal plane are measured with a mechanical anemometer composed by a velocity sensor (Nuova Ceva Automation ANTC-V1) and a direction sensor (ANTC-D1), showed in Fig. 14. The environmental sensors provide the information required to determine the disturbance torques acting on the SMAV. The frequency distribution of both the aerodynamic torque and wind direction are estimated from the collected data. It appears that almost all the wind gusts experienced during the flight were limited below 0.05 Hz. During the design phase, a worst case torque of 30 mNm was assumed and this value matches the peak torques extracted from flight data (see Fig. 15). This peak value was experienced by the SMAV during the ascent and descent phases. The majority of the flight was characterized by torques below 5 mNm with peaks at 10 mNm. More, during the floating phase, the disturbance torque was extremely low and hard to determine. The disturbance was always within the nominal rejection capability of the motion control subsystem.

The external ambient temperature is measured by means of a PT100 thermal sensor. External temperature conditions were harsh during BEXUS-17 flight, and recorded data were as low as −58 °C. However, since it was not possible

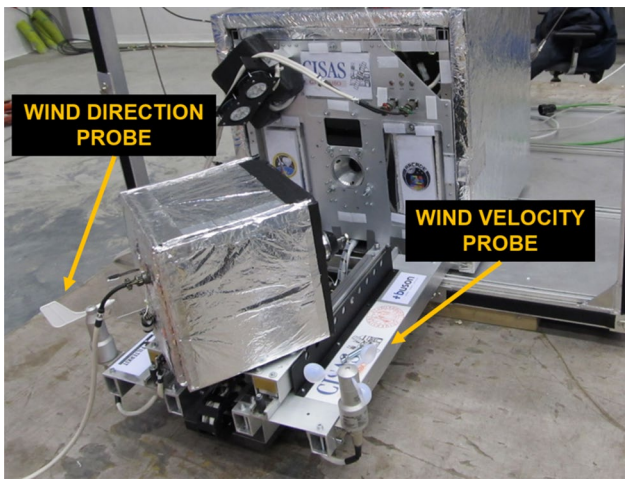

Fig. 14 Wind direction and velocity probes mounted on the experiment

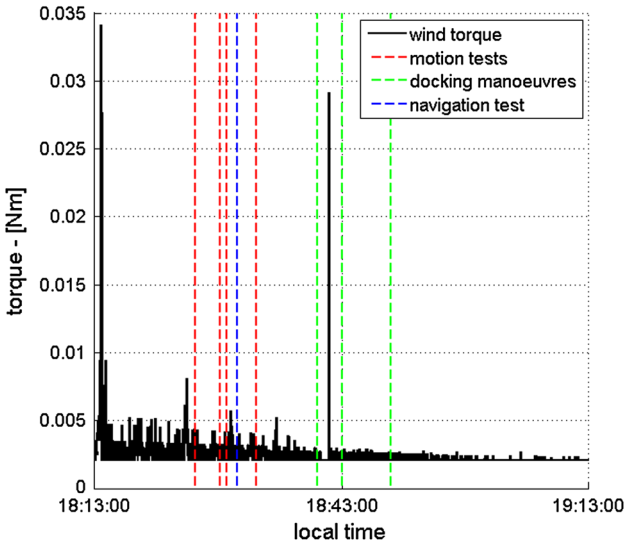

Fig. 15 Estimated wind torques experienced by ARCADE-R2 during the BEXUS-17 flight. Main mission operations are reported

to completely avoid conductive fluxes between the structure and the sensor, the measured temperature profile is probably slightly different from the actual air temperature.

Aiming to gather the information on the atmospheric density and altitude, an absolute pressure sensor (Honeywell SSC DANN 030PAAA5) completes the environmental sensor suite. The minimum atmospheric pressure recorded was 10 mbar, reached during the floating phase. The pressure time profile shows no saturation of the sensor. A good accordance (± 3 % mean error) was achieved between the altitude profile recorded by the E-Bass GPS sensor and that obtained from the measured absolute pressure.

7 Conclusions

ARCADE-R2 is a technology demonstrator experiment that aimed to prove the feasibility of small-scale satellite and/or aircraft systems with automated (a) attitude determination, (b) control and (c) docking capabilities. The experiment consists of a 2-DoF moving vehicle and a fixed assembly with a docking interface; it flew on board the BEXUS-17 stratospheric balloon on October 10, 2013. During the flight, several navigation-control-docking sequences were executed and data on the external pressure, temperature, wind speed and direction were collected, characterizing the atmospheric loads applied to the vehicle.

ARCADE-R2 successfully performed three release operations and two docking procedures running the programmed sequence. The positive results allow stating the total success of the docking subsystem, whose mechanism showed its intrinsic robustness.

A custom infrared sensor for relative navigation was tested during several automatic procedures executed by the experiment, providing real-time estimation of the vehicle distance and attitude with respect to the fixed assembly. The average accuracy of the estimates is, respectively, 5 mm and 1.5°, satisfying the design requirements.

The control system was tested with different combinations of actuators (i.e. reaction wheel and backup DC motor), algorithms (i.e. SS and PID controllers) and sensors (i.e. custom IR sensor and optical encoder). The control system behaved properly in all cases relying on encoder feedback.

The ARCADE-R2 experiment and the positive results from BEXUS-17 flight set an important baseline for future development in the field of docking and rendezvous technologies for small autonomous vehicles and is currently a valuable technology asset in the research activities of the Centre of Studies and Activities for Space “G. Colombo”—(University of Padova).

References

1. On-Orbit Satellite Servicing Study, Project Report, NASA (2010)
2. Saleh, J.H., Lamassoure, E., Hastings, D.E.: Space system flexibility provided by on-orbit servicing: part I. J. Spacecr. Rockets. **39**(4), 551–560 (2001)
3. Rodgers L.: Concepts and technology development for the autonomous assembly and reconfiguration of modular space systems. Master Thesis, Massachusetts Institute of Technology (2005)
4. Gralla E.L.: Strategies for launch and assembly of modular spacecraft. Master Thesis, Massachusetts Institute of Technology (2006)
5. Nishida, S.I., Kawamoto, S., Okawa, Y., Terui, F., Kitamura, S.: Space debris removal system using a small satellite. Acta. Astronaut. **65**, 95–102 (2009)
6. Kaplan M.H.: Space debris realities and removal. In: Proceedings of the 16th Improving Space Operations Workshop (2010)
7. Miller D., Saenz-Otero A., Wertz J. et al.: SPHERES: a testbed for long duration satellite formation flying in micro-gravity conditions. In: Proceedings of the AAS/AIAA Space Flight Mechanics Meeting (2000)
8. Rodgers L., Hoff N., Jordan E., Heiman M., Miller D.W.: A universal interface for modular spacecraft. In: Proceedings of 19th Annual AIAA/USU Conference on Small Satellites (2005)
9. Tchoryk P., Hays A.B., Pavlich J.C.: A docking solution for on-orbit satellite servicing: part of the responsive space equation. In: Proceedings 1st Responsive Space Conference (2003)
10. Ui, K., Matunaga, S., Satori, S., Ishikawa, T.: Microgravity experiments of nano-satellite docking mechanism for final rendezvous approach and docking phase. Microgravity. Sci. Technol. **17**(3), 56–63 (2005)
11. Boesso, A., Francesconi, A.: ARCADE small-scale docking mechanism for microsatellites. Acta. Astronaut. **86**, 77–87 (2013)
12. Olivieri L., Francesconi A.: Design of a docking mechanism for small spacecraft. In: Proceedings 63rd International Astronautical Congress (2012)
13. Olivieri L., Branz F., Savioli L., Francesconi, A.: Conceptual design of small spacecraft docking mechanism actuated by

electroactive polymers. In: Proceedings 2nd IAA Conference on University Satellites Missions and Cubesat Winter Workshop (2013)
14. Olivieri L., Antonello A., Savioli L., Francesconi A.: Dynamic behavior of a semi-androgynous small satellite docking interface. In: Proceedings 65rd International Astronautical Congress (2014)
15. Wenzel, K.E., Masselli, A., Zell, A.: Automatic take-off, tracking and landing of a miniature UAV on a moving carrier vehicle. J. Intell. Rob. Syst. **61**, 221–238 (2010)
16. Meier L., Tanskanen P., Fraundorfer F., Pollefeys M.: Pixhawk: a system for autonomous flight using onboard computer vision. In: Proceedings IEEE International Conference Robotics and Automation (2011)
17. Kendoul, F., Fantoni, I., Nonami, K.: Optic flow-based vision system for autonomous 3D localization and control of small aerial vehicles. Robotics. Auton. Syst. **57**, 591–602 (2009)
18. Grzonka S., Grisetti G., Burgard W.: Towards a navigation system for autonomous indoor flying. In: Proceedings IEEE International Conference on Robotics and Automation (2009)
19. Sansone, F., Branz, F., Francesconi, A., Barbetta, M., Pelizzo, M.G.: 2D close range navigation sensor for miniature cooperative spacecraft. IEEE. Trans. Aerosp. Electron. Syst. **50**(1), 160–169 (2014)
20. Levenberg, K.: A method for the solution of certain non-linear problems in least squares. Q. Appl. Math. **2**, 164–168 (1944)
21. Marquardt, D.W.: An algorithm for least-squares estimation of nonlinear parameters. J. Soc. Ind. Appl. Math. **11**(2), 431–441 (1963)